Title:

Hemodynamic transient and functional connectivity follow structural connectivity and cell type over the brain hierarchy

Kai-Hsiang Chuang[1,2*], Helena H Huang[1], Shabnam Khorasani Gerdekoohi[1], Zengmin Li[1], Dilsher Athwal[1]

[1] Queensland Brain Institute, [2] Centre for Advance Imaging, The University of Queensland, Brisbane, Australia

Running title: Structure-function in brain hierarchy

Keywords: brain connectome, functional MRI, axonal connectivity, excitatory and inhibitory neuron, structure-function relationship

***Address correspondence to:**
Kai-Hsiang Chuang, Ph.D.
Queensland Brain Institute
The University of Queensland
Brisbane, Queensland 4072, Australia
Email: kaichuang@gmail.com

Abstract

The neural circuit of the brain is organized as a hierarchy of functional units with wide-ranging connections that support the information flow and functional connectivity. Studies using magnetic resonance imaging (MRI) indicate a moderate coupling between structural and functional connectivity at the system level. However, how do connections of different directions (feedforward and feedback) and regions with different excitatory and inhibitory (E/I) neurons shape the hemodynamic activity and functional connectivity over the hierarchy are unknown. Here, we used functional MRI to detect optogenetic-evoked and resting-state activities over a somatosensory pathway in the mouse brain and compared with axonal projection and E/I distribution. With a highly sensitive ultrafast imaging, we identified extensive activation in regions up to the third order of axonal projections following optogenetic excitation of the ventral posteriomedial nucleus of the thalamus. The evoked response and functional connectivity correlated with feedforward projections but less with the feedback and weakened with the hierarchy. The hemodynamic signal exhibited regional and hierarchical differences, with slower and more variable responses in high-order areas and bipolar responses predominantly in the contralateral cortex. Importantly, the positive and negative parts of hemodynamics correlated with E/I neuronal densities, respectively. Furthermore, resting-state functional connectivity more associated with E/I distribution whereas stimulus-evoked effective connectivity followed structural wiring. These findings indicate that structure-function relationship is projection-, cell-type- and hierarchy-dependent. Hemodynamic transients could reflect E/I activity and the increased complexity of hierarchical processing.

Significance statement

The neural circuit of the brain is organized as a hierarchy of functional units with complicated feedforward and feedback connections to selectively enhance (excitation) or suppress (inhibit) information from massive sensory inputs. How brain activity is shaped by the structural wiring and excitatory and inhibitory neurons are still unclear. We characterize how brain-wide hemodynamic responses reflect these structural constituents over the hierarchy of a somatosensory pathway. We find that functional activation and connectivity correlate with feedforward connection strengths and neuronal distributions. This association subsides with hierarchy due to slower and more variable hemodynamic responses, reflecting increased complexity of processing

and neuronal compositions in high-order areas. Our findings indicate that hemodynamics follow the hierarchy of structural wiring and neuronal distribution.

Introduction

Decoding information processing over the highly interconnected brain network requires knowledge of the hierarchy organization of its structural connectivity (SC) and structure-function relationship. Elucidating how structure and function are coupled or deranged is not only fundamental for uncovering the neural mechanisms of behaviors, cognition and disability (1, 2), but also for early diagnosis and guiding therapeutic interventions, such as neuromodulation (3). Using magnetic resonance imaging (MRI), studies in humans have revealed that SC and functional connectivity (FC) are generally coupled at the system level (4, 5). However, the FC-SC correlation reported in the literature is highly divergent, with SC generally only explaining or predicting ~30% of the variance of functional dynamics (4, 5).

The discrepancy could be partly due to the lack of critical information such as directionality, synaptic density or excitability as MRI measures are surrogate readouts of axonal connection and neural activity. Compared with gold-standard axonal projections determined by injecting tract tracers into the mouse brain (6, 7), the SC estimated by diffusion MRI is only consistent at the system level (8). The resting-state FC simulated is also less predictable without the directionality of the SC (9). Resting-state FC measured by blood oxygenation level dependent (BOLD) functional MRI (fMRI) is highly correlated with axonal connectivity in the cortex but not subcortical areas (10–13). Despite strong and reciprocal projections between the thalamus and cortex, the FC is absent. On the other hand, strong FC is seen in regions without a direct projection, indicating an involvement of multi-synaptic connections. Nonetheless, the lack of directionality in FC analysis makes it difficult to locate the corresponding pathways. Task- or stimulus-evoked fMRI would allow the effective connectivity to be estimated, but this relies on a clear understanding of the regional hemodynamic response function (HRF) (14) as BOLD responses are variable across regions (15–17). Besides a timing dependency on the vasculature (18), excitatory and inhibitory (E/I) neurons have different contributions to the neurovascular coupling, hence shaping the regional HRF (19–22). How BOLD signal represents underlying E/I activity, hierarchy and axonal projections remains unclear. Regional E/I activity estimated by magnetic resonance spectroscopy has been associated with evoked and spontaneous BOLD amplitude and FC (23–25). However, due to the low sensitivity, the measurement is typically restricted to a selected region. How FC relates to brain-wide E/I neuronal organization is unknown.

To understand the structure-function coupling in brain hierarchy, we focused on the well-studied somatosensory pathway. In rodents, tactile information from the head, nose and whiskers is conveyed to the primary somatosensory cortex (SSp) via the thalamocortical projection from the ventral posteromedial nucleus (VPM) in the thalamus (7, 26). The SSp sends feedforward projections to the ipsilateral sensory, motor and association cortices, to the contralateral somatomotor cortices, and to subcortical areas, including the basal ganglia and midbrain. It also projects back to the ipsilateral thalamus via the corticothalamic projection, forming a closed loop (27). Whereas the electrophysiological properties and cell-type organization of the VPM projection to the somatosensory cortex have been studied extensively (28), structure-function relationship in high-order areas is elusive, partly due to limited brain coverage of neural recordings and optical imaging. fMRI is a powerful tool for mapping whole-brain activity. Activation in the somatosensory pathway has been reliably detected in anesthetized and awake mice (29–31). Nonetheless, activation in high-order areas predicted by the SC, such as the contralateral SSp and association areas, have rarely been found because of low detection sensitivity (32, 33).

Here we investigated how directed SC and E/I organizations shape BOLD responses and FC over the hierarchy of a somatosensory pathway using optogenetic and resting-state fMRI. Compared to sensory stimulation, optogenetic excitation of the VPM allows dissecting downstream responses while avoiding task-specific effects and bypassing processing in precedent regions, such as the brainstem (34). To address the sensitivity issue, we developed an ultrafast imaging that depicts whole-brain hemodynamics with 80% higher sensitivity (35). Together with axonal projection and cellular distribution mapping of the mouse brain (6, 36), we found that BOLD signal changed with hierarchy and local E/I activity. Whereas FC coupled with both the SC and E/I organization, they had differential contributions during evoked and resting states.

Results

Ultrafast fMRI detects brain-wide activation.

To selectively activate the VPM, AAV5-hSyn-ChR2(H13R)-eYFP-WPRE was stereotaxically injected into the mouse brain to express channelrhodopsin-2 (ChR2) in all neurons. To detect activation of the VPM pathway, BOLD signal was measured by a simultaneous multi-slice echo-planar imaging that covered the entire cerebrum with 0.3s temporal resolution. Fig. 1A shows that the optic fiber targeted the dorsal VPM with low distortion despite signal loss due to a susceptibility artifact around the fiber.

Histology revealed good expression of ChR2 in the VPM (Fig.1B). As stimulation frequency has a strong influence on the spatial extent of the activation (37), we evaluated the effects of stimulating light frequency and intensity in randomized orders: 4 frequencies from 1, 5, 10 to 20 Hz were delivered in 9.9s blocks, and 5 intensities from 0.3, 0.5, 1.0, 1.25 to 2.0 mW at 5Hz were delivered as 1.5s events to minimize neural adaptation in the block design (Fig. 1C).

After preprocessing to remove nuisance, co-registering to the Allen Brain Atlas space, and analyzing by a general linear model, our results revealed far-reaching activation in the isocortex (ISO), thalamus (TH), midbrain (MB) and hindbrain (HB), with sparse activation in the striatum (STR), pallidum (PAL), hippocampal formation (HPF) and hypothalamus of both hemispheres (Fig. 1D). With decreased stimulation intensity, the activation became restricted to the ipsilateral TH, bilateral VPM, bilateral motor-related superior colliculus (SCm) and part of the visual cortex (Fig. 1E). Similarly broad activation was seen at 1 and 5 Hz stimulations (supplementary Fig. S1), consistent with previous studies in rats (37). Less cortical activation was seen at 10Hz. At 20Hz, the subcortical activation was reduced and more restricted to the ipsilateral TH and the SCm. Interestingly, negative BOLD responses were consistently found in the contralateral cortex at all the stimulation frequencies. This demonstrated the detection of downstream activation throughout the brain with enhanced fMRI sensitivity.

Activation matches SC hierarchy.

We constructed the system-level hierarchy across 350 brain regions based on axonal projections derived from the monosynaptic anterograde tract tracing data in the Allen Brain Connectivity atlas (6). SC strength was calculated as the summed axonal projection volumes, normalized by the tracer injection volume. From the VPM, there was up to 74 target areas, distributed in the ISO, TH, MB and HB, which receive direct (first-order) projections (supplementary Fig. S2A). The strongest projections are the secondary somatosensory cortex (SSs) and the upper lip (SSpul), mouth (SSpm), nose (SSpn) and barrel field (SSpbfd) in the SSp, reticular nucleus of the thalamus (RT) and SCm of the ipsilateral hemisphere. There were also contralateral projections to the above somatosensory areas, but the projection strengths were at least 68-fold weaker. From the somatosensory cortex, much broader second-order connections could be found. For example, the SSpbfd projected to 233 regions (supplementary Fig. S2B), with strong feedforward projections to the ipsilateral caudate putamen, primary motor cortex (MOp), secondary motor cortex (MOs) and SSs, and to the contralateral barrel field ($SSpbfd_c$), as well as feedback projections to the VPM and posterior complex of thalamus.

The hierarchy could be better visualized by removing weak connections. As the SC follows a lognormal distribution (6), a threshold was defined based on the logarithm of the SC (supplementary Fig. S2C). By choosing the top 10% strongest connections, the hierarchy showed that the major first-order areas are in the ipsilateral somatosensory cortex (supplementary Fig. S2D). The second-order afferents included feedforward projections to other sensory and motor areas in both hemispheres and feedback projections to the ipsilateral somatosensory areas and thalamus. The third-order afferents extended to limbic and association areas, such as the anterior cingulate area. The peak amplitude of the evoked BOLD responses in each region was tested and showed significant change ($p<0.01$ uncorrected) in >96% of the regions predicted by the SC. Compared to this structural hierarchy, up to third-order areas could be identified by fMRI.

Cortical responsiveness and timing change with hierarchy.

To understand how hemodynamic responsiveness changes with hierarchy, the evoked BOLD responses of different stimulation intensities were inspected (Fig. 2A). The VPM activation increased with stimulation intensity and reached a plateau at around 1.25 to 2 mW. The responses in the first-order cortical areas, such as the SSpbfd and SSs, followed a similar trend but plateaued slightly earlier. In the second-order areas, such as the MOp, the activation was weaker and had a different trend. This was more apparent when fitting the peak BOLD responses by a sigmoidal function (Fig. 2B). Compared to the sigmoid trend in the VPM, those in the TH and MB were highly similar ($r=0.99\pm0.003$, mean±standard error) regardless of the hierarchy. In contrast, those in the ipsilateral ISO were variable ($r=0.89\pm0.058$) and more divergent in the contralateral ISO ($r=0.59\pm0.17$). The cortical intensity response curves became more variable with hierarchy (supplementary Fig. S3), suggesting increased complexity of regional processing in higher-order areas. As the cortical activation tends to plateau above 1mW, the peak BOLD amplitude at 1mW stimulation was assessed. The BOLD amplitudes reduced with hierarchy ($F_{3,63}=17.21$, $p<0.0001$), with activations in the second-order ISO significantly weaker ($p<0.0001$) than that of the first-order somatosensory area (Fig. 2C). The more variable and weaker activation in high-order cortical areas may explain their poor detectability in previous studies.

Knowing the precise HRF is critical for analyzing and interpreting hemodynamic-based functional imaging and for modeling brain dynamics. Previous studies in rodents showed that HRFs of different cortical areas are generally the same (31, 38). Intriguingly, we found distinct BOLD responses in subcortical and cortical regions (Fig. 3A). BOLD responses were similarly sharp in the TH and MB, slightly broad in ISO, but slow in the STR and PAL. In particular, biphasic responses were

consistently found in the contralateral cortex but not subcortical regions. These responses were not dependent on the hierarchy as the second-order ipsilateral areas, such as the MOp, still showed a positive response (Fig. 3B). To characterize regional BOLD responses, the signals were fitted with double gamma variate functions. Based on the hierarchy of major projections, the responses were more variable at higher order (Fig. 3C). The time-to-rise, defined as the time when a signal increase to 30% of the peak, in the higher order areas were significantly longer than those in the first-order areas ($F_{2,21}$=4.93, p=0.017; Fig. 3D). The time-to-positive-peak in the ipsilateral cortex also increased over the hierarchy ($F_{2,20}$=5.45, p=0.013) from 2.48±0.14 (mean±standard error) to 3.51±0.32 s (Fig. 3E). The responses in the contralateral cortex had shorter time-to-positive-peak but longer time-to-negative-peak than the peak timing in the ipsilateral cortex of the same hierarchy. However, these contralateral peak timings were not hierarchy dependent. These results suggest that initial timing of BOLD responses could reveal hierarchical relationship.

Time-lag regression analysis, such as Granger causality, has been used for estimating causality. To test whether BOLD timing could be estimated by regression, we used cross-correlation analysis to estimate the BOLD signal lag time with respect to the VPM. Surprisingly, the lag time did not correlate with the time-to-rise or time-to-peak, but did correlate with peak BOLD amplitude (r=-0.4, p<0.0001; supplementary Fig. S4). The lag time did show a trend (Kruskal-Wallis statistics=6.88, p<0.05) of increase over the hierarchy in the ipsilateral cortex, likely due to hierarchy-dependent reduction of the BOLD amplitude. This indicates that although time-lag analysis may show hierarchy dependent change, it does not reflect the actual hemodynamic timing.

BOLD activation and FC correlate with feedforward projection.

To understand how SC influences BOLD activities, we compared their relationship over the thalamocortical (feedforward), corticocortical (feedforward and feedback) and corticothalamic (feedback) projections (Fig. 4A). In the thalamocortical projection, the peak BOLD amplitudes in the targeted cortical areas highly correlated with the SC from the VPM (R^2=0.77, p=6.4x10^{-5}; Fig. 4B). However, the BOLD activation in the subcortical areas (TH, MB and HB) was not associated with feedforward from the VPM. The corticocortical feedforward from most of the somatosensory areas to the ipsilateral cortex also correlated with the BOLD activation in these second-order areas with R^2 ranging from 0.16 to 0.79 (Fig. 4C). However, we observed no association in the corticocortical feedforward to the contralateral cortex, except the interhemispheric somatosensory areas (R^2=0.88, p<0.05; Fig. 4D). There was also no association in corticocortical feedback among the somatosensory areas. In

the corticothalamic feedback, we found that the thalamic BOLD activation correlated with the SC from the SSpbfd and SSpm (Fig. 4E), but not the other somatosensory areas. Notably, the association with feedforward SC was not observable in the block-design data (supplementary Fig. S5). The proportionally higher BOLD response over stronger SC supports typical assumption of neural modeling that regional activation depends on the projection strength. However, this coupling varied among projections, diminished in feedback projections, and abolished by nonlinear effects under a longer stimulation.

To determine the FC-SC coupling, we calculated the FC by zero-lag correlation coefficients between regional time-courses under optogenetic stimulation (FC_{Task}) or resting state (FC_{Rest}). Unlike FC_{Rest}, which showed strong cortical but weak subcortical connectivity, the FC_{Task} was strong within and between the TH and MB (Fig. 5A). On the other hand, the interhemispheric cortical FC_{Task} was weak due to the hemodynamic difference between hemispheres. Despite these differences, the FC_{Rest} highly correlated with FC_{Task} over the whole brain (R^2=0.62), ISO (R^2=0.57, p=7.9x10^{-67}) and TH (R^2=0.81, p=8.1x10^{-156}).

The FC_{Task} correlated with the SC in the thalamic (R^2=0.35, $p<0.05$) and thalamocortical (R^2=0.84, $p<0.0001$) feedforward from the VPM (Fig. 5B). In the cortex, the FC_{Task} correlated with the corticocortical feedforward within and between hemispheres with R^2 = 0.23 to 0.84 (Fig. 5C). In comparison, FC_{Rest} only correlated with SC in a few connections. However, neither FC_{Task} nor FC_{Rest} correlated with the SC in the corticothalamic feedback (Fig. 5D). There was also slight trend of decrease FC over hierarchy (Fig. 5E) which could be due to weaker and more variable BOLD responses at higher order. These results show that FC_{Task}, but not FC_{Rest}, has moderate to high correlation with directed SC, particularly in the feedforward projections.

Cortical evoked response and FC associate with E/I organization.

Previous studies of spatial association between FC and gene expression pattern suggested cellular organization and micro-circuitry may underlie the correlation (39). However, whether regional E/I compositions contribute to the differences in evoked response and FC is unclear. We extracted the neuronal densities of the excitatory neurons and 3 major types of inhibitory interneurons that express somatostatin (SST^+), parvalbumin (PV^+), and vasoactive intestinal peptide (VIP^+), respectively (36, 40). Linear regression was used to predict hemodynamic parameters, including timing, amplitude and width, based on the neuronal densities. We found that excitatory, but not inhibitory, neuronal density contributed to the time-to-peak (R^2=0.18, p=0.0077) and full-width-at-half-maximum (FWHM; R^2=0.11, p=0.039) of the positive BOLD responses in the cortex (Fig. 6A). The time-to-rise and FWHM of

the negative BOLD responses were influenced by the densities of inhibitory SST^+ (R^2=0.36, p=0.0037) and VIP^+ (R^2=0.59, p=0.00005) neurons, respectively (Fig. 6B). On the contrary, the hemodynamic parameters of subcortical areas, such as the TH, did not correlate with any of the neuron types. Interestingly, E/I ratio, calculated by dividing the excitatory neuron density by the sum of the 3 types of inhibitory neurons, increased over the hierarchy (Kruskal-Wallis statistic=9.495, p=0.0087) due to decreased SST^+ ($F_{2,48}$=4.14, p=0.022) and PV^+ ($F_{2,48}$=4.09, p=0.023) neuronal densities over the hierarchy of major connections (supplementary Fig. S6). This partly explained the hierarchy-dependent signal variation as the cortical BOLD similarity decreased with E/I ratio (ρ=-0.28, p=0.013; supplementary Fig. S6C). These results suggest that hemodynamic characteristics may reflect underlying E/I activity.

To understand whether E/I distribution contributed to the connectivity, we estimated the inter-regional similarity of the E/I distribution by correlating the normalized neuronal density profiles between regions to create an E/I similarity matrix (Fig. 6C). The HPF has the most similar E/I distribution (r=0.89±0.12), followed by ISO (r=0.63±0.44). In contrast, the TH (r=0.25±0.66), MB (r=0.29±0.63), and STR (r=0.21±0.76) had heterogeneous neuron types. Within the ISO, the E/I similarity within functional modules is generally higher than between modules (supplementary Fig. S7A). For instance, E/I similarity was 0.84±0.16 and 0.93±0.078 within the somatosensory and visual cortex, respectively. But similarity between the somatosensory and visual cortex was 0.65±0.30. The heterogeneity was mainly driven by the excitatory neuron as the inter-regional similarity of inhibitory neuronal density was generally high (supplementary Fig. S7B,C).

Compared with the cortical FC (Fig. 6D), there was weak correlations between E/I similarity and FC_{Rest} (ρ=0.26, p=3.8×10^{-10}) and FC_{Task} (ρ=0.27, p=2×10^{-7}) within hemisphere, though less between hemispheres (FC_{Rest} ρ=0.20, p=1.5×10^{-5}; FC_{Task} ρ=0.21, p=0.013). Interestingly, regions with similar E/I distribution also tended to have stronger SC (Fig. 6E), including the thalamocortical (ρ=0.23, p=0.039) and corticocortical (ρ=0.35, p=0.00097 intra-hemisphere; ρ=0.35, p=0.00026 inter-hemisphere) feedforward projections, and the corticothalamic feedback (ρ=0.45, p=0.000026). To determine whether SC or E/I distribution more contributed to FC, we used either or both factors as predictors of FC in a linear model (supplementary Table S1). The goodness-of-fit R^2 to the cortical FC_{Rest} increased when using E/I similarity alone or together with the SC, whereas the prediction of FC_{Task} only had marginal improvement. These results indicate that cortical regions of similar neuronal compositions tended to connect with each other. Particularly, FC_{Rest} was more dependent on E/I distribution, while FC_{Task} more on the SC.

Discussion

This study evaluated two structural constituents, axonal projection and E/I neurons, of the system-level functional dynamics over the hierarchy of a somatosensory pathway. We found that evoked BOLD responses and FC_{Task} correlated with feedforward projection and E/I distribution. The association subsided with hierarchy due to weaker and more variable activation in higher order areas. These characteristics became obscure when the evoked responses were less linear. We also found that hemodynamic timing and shape reflected E/I neuronal density and hierarchy, which would provide information of regional processing and information flow, respectively. Particularly, we discovered that cortical regions with similar E/I distributions had stronger SC and FC, with FC_{Rest} more corresponded to E/I similarity and FC_{Task} more aligned with the SC. This greatly expands previous studies which only examined the first-order projection on the cortical surface (41) or undirected connectivity (10–13). The findings that BOLD transients follow the SC and E/I distribution support the use of hemodynamic signals to probe system-level brain network dynamics and to infer causality. The variable hemodynamic response indicates a need to refine current hemodynamic model for data analysis, neural modeling, and interpretation.

We demonstrated that ultrafast fMRI allowed the detection of brain-wide hemodynamic transients under short stimulus events which improved characterization of structure-function relationships. Previous fMRI studies mostly detected activation in the ipsilateral somatosensory cortex (42), likely due to the anesthesia effects (43, 44), a weak thalamic response (45) and insufficient sensitivity (29, 46). Limited downstream responses were reported even with direct optogenetic stimulations of the cortex (47) or the thalamus (48). With improved sensitivity provided by a cryogenic coil or ultrahigh field MRI, more activation was recently observed in awake (31) and anesthetized mice (29, 32, 49). Although traditional block design could increase sensitivity, it made responses more nonlinear and harder to associate with the SC.

The weaker and more variable BOLD responses in high-order areas is consistent with an increased activity timescale (50) and variation of latency (51) over the hierarchy. A slower hemodynamics in high-order areas accords with recent studies which showed that initial transients of BOLD responses can reflect neural information flow in the visual and somatosensory pathways (32, 52, 53). However, the relationship between neuronal and hemodynamic timing remains unclear. Such hierarchy-dependent dynamics could originate from multi-synaptic connections which lead to longer "temporal receptive window" in high-order association areas but shorter activity in

the sensory cortex (54). This was recently identified in humans using resting-state fMRI (55).

We found distinct evoked responses among structural organization and hierarchy, with the hemodynamic timing in the STR/PAL slower than other regions. Such brain structure-dependent hemodynamics could be due to activation of different cell types owing to different projected targets and cellular distributions (56). Specifically, a biphasic response was only seen in the contralateral cortex. Transcallosal interhemispheric inhibition plays an important role in sensory processing, motor control and neuroplasticity (57, 58) by excitatory efferent from the ipsilateral cortex to the local interneurons in the contralateral hemisphere. How inhibitory activity manifests in the BOLD signal is still uncertain. Although a negative BOLD signal would be expected, previous studies also reported a positive response (58, 59). Recent studies found biphasic BOLD or blood flow responses by optogenetic activation of inhibitory neurons, particularly the SST^+ neurons (21, 60). We also found that negative BOLD associated with inhibitory neuronal densities. These together indicate that negative BOLD reflects transcallosal inhibition. A previous study showed bilateral positive activation under VPM excitation in isoflurane-anesthetized rat (37). This is likely due to isoflurane effects on E/I activity (61).

Both evoked activation and FC correlated with feedforward, but less with feedback, projections. Although this may be due to the suppression of cortical feedback by anesthesia (62), a study in awake monkey found that thalamocortical feedforward spiking activity increases with stimulus intensity whereas corticothalamic feedback remains unchanged (63). This may be due to the interaction of multiple feedback information and the function of a feedback route. While corticothalamic projections are mostly excitatory, they could also induce inhibition via the RT (64). In the sensory pathway, feedback signals have diverse modulatory roles in behaviors, such as attention, than delivering sensory information in the feedforward (65). Further differentiation of excitatory versus inhibitory connections will help to clarify the weak coupling in feedback projections.

We found that E/I ratio increased over the hierarchy and may underlie the increased BOLD variability. This is consistent with macroscopic gradient of E/I distribution and top-down control of sensory inputs (66). We also found that E/I similarity correlated with both structural and functional connectivity and was a major contributor of the FC_{Rest}. Incorporating this information may improve modeling and predicting neural dynamics. Why regions with similar E/I distribution have stronger SC and FC is

unclear. This may be due to similar genetic profile and developmental origin. For instance, cortical excitatory neurons originated from the same progenitor cell have stronger synaptic connections, share similar stimulus selectivity and form long-range connections with the same microcircuit in high-order area (67, 68).

There are several limitations of this study. Although we used one of the most reliable anesthesia protocols for mouse fMRI, the anesthesia could affect both neural and hemodynamic responses in pathways involving thalamic and limbic areas (69). This issue would be minimized by further development of awake fMRI that incorporate optogenetics (70). Secondly, we activated all neurons to allow comparison with the SC that does not differentiate cell types. As different types of neurons have preferential projections, activated regions can be cell-type dependent (56). Further study using cell-type-specific projections and stimulations would allow the delineation of a more precise relationship in excitatory and inhibitory connections. Thirdly, the interhemispheric FC_{Task} was underestimated due to the distinct hemodynamic response in the contralateral cortex. Deconvolution of the response function may improve the estimation but this requires high signal-to-noise ratio. Finally, due to the limited spatial resolution, the cortical layer was not differentiable. Pushing the spatial resolution using higher field MRI will enable comparison with laminar input-output projections (71) and E/I distribution to further understand the structure-function relationship at the mesoscale.

Materials and Methods

Experimental Design

Animal experiments were approved by the Animal Ethics Committee of the University of Queensland. Three groups of male C57BL6/J mice were used: one for evaluating the heating effects of optogenetic stimulation (n=6 with ChR2 and n=3 without virus), the second (n=8) for investigating responses to different stimulus intensities and frequencies, and the third was naïve group (n=11) without surgery for acquiring resting-state fMRI. The mice were aged 6-7 weeks at the time of viral injection and 9-15 weeks at the time of fMRI.

Surgical procedures

A small craniotomy was made under 2% isoflurane. AAV5-hSyn-ChR2(H13R)-eYFP-WPRE was injected into the brain at A/P: -1.82mm, M/L: 1.5mm (left), D/V: 3.3mm, relative to bregma using Nanoject III (Drummond). A ceramic fiber-optic cannula (200μm core, RWD) was inserted and fixed by dental cement.

Stimulation design

Blue light (470nm) pulses with intensities of 0.3, 0.5, 1, and 2 mW, corresponding to 9.5, 16, 32, 64 mW/mm^2 peak power, were delivered (ON: 1.5s; OFF: 10.5s; pulse duration: 20ms; 5Hz) each repeated 10 times in a randomized order, corresponding to a duration of 495s (1650 volumes) per run. This was repeated 2-3 times in each animal. Another stimulus intensity of 1.25mW (=40 mW/mm^2) that matches that used in a previous study in rats (37) was examined in a separate run (1.5s on and 10.5s off, repeated 30 times) without intermixing with other intensity levels, corresponding to a duration of 1250 volumes.

4 stimulus frequencies of 1, 5, 10 and 20 Hz (power: 1mW, pulse duration: 20ms) were delivered in a randomized order as a block design with an initial rest period of 15s and a stimulation duration of 9.9s, followed by an interstimulus rest period of 40.2s. Each frequency was repeated 4 times during the protocol, corresponding to a duration of 816.6s (2722 volumes) per run.

MRI

MRI was conducted on a 9.4T pre-clinical scanner (Bruker BioSpin MRI GmbH) under 0.1mg/kg/h medetomidine and 0.2-0.5% isoflurane as described previously (35). After localized high-order shim, structural MRI was acquired with 0.1x0.1x0.3mm^3 resolution. Functional data were acquired using a 4-band gradient-echo echo-planar imaging with TR/TE=300/15ms, 16 slices,

thickness/gap=0.5/0.1mm, in-plane resolution=300μm and 7/8 partial-Fourier (35). Non-accelerated reverse phase-encoding EPI was acquired for distortion correction. To ensure proper neurovascular coupling, visual activation was examined (35) prior to optogenetic experiments.

Histology

After the last MRI session, animals were perfused transcardially with 4% paraformaldehyde followed by brain extraction for histology.

MRI data processing

Data were processed using our optimized data processing pipeline (72) and registered to the Allen Mouse Brain template space (73) using nonlinear transformations. Spatial smoothing of a 0.6-mm Gaussian kernel was applied. Task fMRI was analyzed using a general linear model with each intensity/frequency modeled as a boxcar waveform convolved by gamma variate function (standard deviation: 2s; mean lag: 4s). The beta maps of repeated runs in each subject were averaged and used for second-level random effect analysis by one-sample t-test. A voxel-level of $p<0.05$, corrected by false discovery rate (FDR), was regarded as significant.

The mean BOLD signals in the regions-of-interest (ROIs), defined based on the brain template (supplementary Table S2), were extracted, averaged over trials and wavelet-denoised to derive the evoked responses. The stimulation responsiveness was determined by fitting the peak BOLD amplitude, S, to a sigmoid function:

$$S(i) = \frac{a}{1+e^{-b(i-c)}} \qquad (1)$$

where i denotes different stimuli, and a, b and c are the fitted parameters. The predictability of regional responsiveness was estimated by linear regression between the intensity-dependent peak BOLD changes. The regional hemodynamic properties were estimated by fitting a double gamma-variate function that convolved with the stimulation paradigm to the evoked BOLD responses of the 2mW stimulation. The hemodynamic response was defined as:

$$HR(t) = a_1 t^{b_1} e^{-t/c_1} - a_2 t^{b_2} e^{-t/c_2} \qquad (2)$$

where t is the time, and a_1, b_1, c_1, a_2, b_2 and c_2 are the fitted parameters. The time-to-rise of an response was defined as the time rising above 30% of the peak amplitude, sampled at 0.1s resolution.

Pearson's correlation coefficients, r, between the ROI time-courses were calculated to generate the FC matrix. Significant connectivity was determined by one-sample t-test of Fisher's z-transformed r, thresholded at $p<0.01$, two-tailed,

uncorrected. The mean *z*-score was converted back to *r* to represent the FC strength. Cross-correlation was calculated with a lag time up to 3s.

Statistical analysis

Correlation was determined by either linear regression or Spearman correlation, ρ, when the trend was not linear. Hierarchy difference was tested by one-way Brown-Forsythe ANOVA with Dunnett's test for multiple comparisons or non-parametric Kruskal-Wallis test with Dunn's test for multiple comparisons when the distribution was skewed (Prism, GraphPad Software). A value of $p<0.05$ was regarded as significant. The results are reported as mean ± standard deviation, unless specifically noted.

References

1. A. Raj, F. Powell, Models of Network Spread and Network Degeneration in Brain Disorders. *Biol. Psychiatry Cogn. Neurosci. Neuroimaging* **3**, 788–797 (2018).
2. M. P. van den Heuvel, O. Sporns, A cross-disorder connectome landscape of brain dysconnectivity. *Nat. Rev. Neurosci.* **20**, 435–446 (2019).
3. A. Horn, M. D. Fox, Opportunities of connectomic neuromodulation. *Neuroimage* **221**, 117180 (2020).
4. M. Straathof, M. R. R. T. Sinke, R. M. Dijkhuizen, W. M. Otte, A systematic review on the quantitative relationship between structural and functional network connectivity strength in mammalian brains. *J. Cereb. Blood Flow Metab.* **39**, 189–209 (2019).
5. L. E. Suárez, R. D. Markello, R. F. Betzel, B. Misic, Linking structure and function in macroscale brain networks. *Trends Cogn. Sci.* **24**, 302–315 (2020).
6. S. W. Oh, *et al.*, A mesoscale connectome of the mouse brain. *Nature* **508**, 207–214 (2014).
7. I. M. Zakiewicz, J. G. Bjaalie, T. B. Leergaard, Brain-wide map of efferent projections from rat barrel cortex. *Front. Neuroinform.* **8**, 1–15 (2014).
8. E. Calabrese, A. Badea, G. Cofer, Y. Qi, G. A. Johnson, A Diffusion MRI Tractography Connectome of the Mouse Brain and Comparison with Neuronal Tracer Data. *Cereb. Cortex* **25**, 4628–4637 (2015).
9. F. Melozzi, *et al.*, Individual structural features constrain the mouse functional connectome. *Proc. Natl. Acad. Sci. U. S. A.* **116**, 26961–26969 (2019).
10. J. Grandjean, V. Zerbi, J. H. Balsters, N. Wenderoth, M. Rudin, Structural Basis of Large-Scale Functional Connectivity in the Mouse. *J. Neurosci.* **37**, 8092–8101 (2017).
11. W.-T. Chang, *et al.*, Connectomic imaging reveals Huntington-related pathological and pharmaceutical effects in a mouse model. *NMR Biomed.* **31**, e4007 (2018).
12. M. Straathof, *et al.*, Distinct structure-function relationships across cortical regions and connectivity scales in the rat brain. *Sci. Rep.* **10**, 56 (2020).
13. J. D. Whitesell, *et al.*, Regional, Layer, and Cell-Type-Specific Connectivity of the Mouse Default Mode Network. *Neuron* **109**, 545-559.e8 (2021).
14. K. Friston, R. Moran, A. K. Seth, Analysing connectivity with Granger causality and dynamic causal modelling. *Curr. Opin. Neurobiol.* **23**, 172–178 (2013).
15. D. A. Handwerker, J. M. Ollinger, M. D'Esposito, Variation of BOLD hemodynamic responses across subjects and brain regions and their effects on

statistical analyses. *Neuroimage* **21**, 1639–1651 (2004).
16. A. M. Puckett, J. R. Mathis, E. A. DeYoe, An investigation of positive and inverted hemodynamic response functions across multiple visual areas. *Hum. Brain Mapp.* **35**, 5550–5564 (2014).
17. D. A. Handwerker, J. Gonzalez-Castillo, M. D'Esposito, P. A. Bandettini, The continuing challenge of understanding and modeling hemodynamic variation in fMRI. *Neuroimage* **62**, 1017–1023 (2012).
18. K. Uludağ, P. Blinder, Linking brain vascular physiology to hemodynamic response in ultra-high field MRI. *Neuroimage* **168**, 279–295 (2018).
19. M. B. Krawchuk, C. F. Ruff, X. Yang, S. E. Ross, A. L. Vazquez, Optogenetic assessment of VIP, PV, SOM and NOS inhibitory neuron activity and cerebral blood flow regulation in mouse somato-sensory cortex. *J. Cereb. Blood Flow Metab.* **40**, 1427–1440 (2020).
20. C. Howarth, A. Mishra, C. N. Hall, More than just summed neuronal activity: how multiple cell types shape the BOLD response. *Philos. Trans. R. Soc. Lond. B. Biol. Sci.* **376**, 20190630 (2021).
21. L. Lee, *et al.*, Key Aspects of Neurovascular Control Mediated by Specific Populations of Inhibitory Cortical Interneurons. *Cereb. Cortex* **30**, 2452–2464 (2020).
22. J. Lee, *et al.*, Opposed hemodynamic responses following increased excitation and parvalbumin-based inhibition. *J. Cereb. Blood Flow Metab.* **41**, 841–856 (2021).
23. R. Rajkumar, *et al.*, Excitatory–inhibitory balance within EEG microstates and resting-state fMRI networks: assessed via simultaneous trimodal PET–MR–EEG imaging. *Transl. Psychiatry* **11**, 60 (2021).
24. N. W. Duncan, C. Wiebking, G. Northoff, Associations of regional GABA and glutamate with intrinsic and extrinsic neural activity in humans A review of multimodal imaging studies. *Neurosci. Biobehav. Rev.* **47**, 36–52 (2014).
25. S. D. Muthukumaraswamy, R. a E. Edden, D. K. Jones, J. B. Swettenham, K. D. Singh, Resting GABA concentration predicts peak gamma frequency and fMRI amplitude in response to visual stimulation in humans. *Proc. Natl. Acad. Sci. U. S. A.* **106**, 8356–61 (2009).
26. R. Aronoff, *et al.*, Long-range connectivity of mouse primary somatosensory barrel cortex. *Eur. J. Neurosci.* **31**, 2221–2233 (2010).
27. G. M. G. Shepherd, N. Yamawaki, Untangling the cortico-thalamo-cortical loop: cellular pieces of a knotty circuit puzzle. *Nat. Rev. Neurosci.* **22**, 389–406 (2021).
28. S. El-Boustani, *et al.*, Anatomically and functionally distinct thalamocortical

inputs to primary and secondary mouse whisker somatosensory cortices. *Nat. Commun.* **11**, 3342 (2020).

29. W. Beom, *et al.*, Mouse BOLD fMRI at ultrahigh field detects somatosensory networks including thalamic nuclei. *Neuroimage* **195**, 203–214 (2019).
30. F. A. Nasrallah, H. Tay, K.-H. Chuang, Detection of functional connectivity in the resting mouse brain. *Neuroimage* **86**, 417–24 (2014).
31. X. Chen, *et al.*, Sensory evoked fMRI paradigms in awake mice. *Neuroimage* **204**, 116242 (2020).
32. W. B. Jung, G. H. Im, H. Jiang, S.-G. Kim, Early fMRI responses to somatosensory and optogenetic stimulation reflect neural information flow. *Proc. Natl. Acad. Sci. U. S. A.* **118**, e2023265118 (2021).
33. B. J. Edelman, *et al.*, High-sensitivity detection of optogenetically-induced neural activity with functional ultrasound imaging. *Neuroimage* **242**, 118434 (2021).
34. C. K. Kim, A. Adhikari, K. Deisseroth, Integration of optogenetics with complementary methodologies in systems neuroscience. *Nat. Rev. Neurosci.* **18**, 222–235 (2017).
35. H.-L. Lee, Z. Li, E. J. Coulson, K.-H. Chuang, Ultrafast fMRI of the rodent brain using simultaneous multi-slice EPI. *Neuroimage* **195**, 48–58 (2019).
36. Y. Kim, *et al.*, Brain-wide Maps Reveal Stereotyped Cell-Type-Based Cortical Architecture and Subcortical Sexual Dimorphism. *Cell* **171**, 456-469.e22 (2017).
37. A. T. L. Leong, *et al.*, Long-range projections coordinate distributed brain-wide neural activity with a specific spatiotemporal profile. *Proc. Natl. Acad. Sci. U. S. A.* **113**, E8306–E8315 (2016).
38. H. Lambers, *et al.*, A cortical rat hemodynamic response function for improved detection of BOLD activation under common experimental conditions. *Neuroimage* **208**, 116446 (2020).
39. A. Fornito, A. Arnatkevičiūtė, B. D. Fulcher, Bridging the Gap between Connectome and Transcriptome. *Trends Cogn. Sci.* **23**, 34–50 (2019).
40. C. Erö, M.-O. Gewaltig, D. Keller, H. Markram, A cell atlas for the mouse brain. *Front. Neuroinform.* **12**, 1–16 (2018).
41. A. Q. Bauer, *et al.*, Effective connectivity measured using optogenetically evoked hemodynamic signals exhibits topography distinct from resting state functional connectivity in the mouse. *Cereb. Cortex* **28**, 370–386 (2018).
42. B. G. Sanganahalli, C. J. Bailey, P. Herman, F. Hyder, Tactile and non-tactile sensory paradigms for fMRI and neurophysiologic studies in rodents. *Methods Mol. Biol.* **489**, 213–42 (2009).

43. F. A. Nasrallah, J. Tan, K.-H. Chuang, Pharmacological modulation of functional connectivity: α2-adrenergic receptor agonist alters synchrony but not neural activation. *Neuroimage* **60**, 436–46 (2012).
44. H.-J. Shim, *et al.*, Mouse fMRI under ketamine and xylazine anesthesia: Robust contralateral somatosensory cortex activation in response to forepaw stimulation. *Neuroimage* **177**, 30–44 (2018).
45. C. Brunner, *et al.*, A Platform for Brain-wide Volumetric Functional Ultrasound Imaging and Analysis of Circuit Dynamics in Awake Mice. *Neuron* **108**, 861-875.e7 (2020).
46. S. D. Keilholz, A. C. Silva, M. Raman, H. Merkle, A. P. Koretsky, Functional MRI of the rodent somatosensory pathway using multislice echo planar imaging. *Magn. Reson. Med.* **52**, 89–99 (2004).
47. F. Schmid, *et al.*, Assessing sensory versus optogenetic network activation by combining (o)fMRI with optical Ca2+ recordings. *J. Cereb. Blood Flow Metab.* **36**, 1885–1900 (2016).
48. J. H. Lee, *et al.*, Global and local fMRI signals driven by neurons defined optogenetically by type and wiring. *Nature* **465**, 788–92 (2010).
49. D. Nunes, A. Ianus, N. Shemesh, Layer-specific connectivity revealed by diffusion-weighted functional MRI in the rat thalamocortical pathway. *Neuroimage* **184**, 646–657 (2019).
50. J. D. Murray, *et al.*, A hierarchy of intrinsic timescales across primate cortex. *Nat. Neurosci.* **17**, 1661–1663 (2014).
51. J.-F. L. Lin, J. Silva-Pereyra, C.-C. Chou, F.-H. Lin, The sequence of cortical activity inferred by response latency variability in the human ventral pathway of face processing. *Sci. Rep.* **8**, 5836 (2018).
52. R. Gil, F. F. Fernandes, N. Shemesh, Neuroplasticity-driven timing modulations revealed by ultrafast functional magnetic resonance imaging. *Neuroimage* **225**, 117446 (2021).
53. X. Yu, C. Qian, D. Chen, S. J. Dodd, A. P. Koretsky, Deciphering laminar-specific neural inputs with line-scanning fMRI. *Nat. Methods* **11**, 55–8 (2014).
54. R. Chaudhuri, K. Knoblauch, M. A. Gariel, H. Kennedy, X. J. Wang, A Large-Scale Circuit Mechanism for Hierarchical Dynamical Processing in the Primate Cortex. *Neuron* **88**, 419–431 (2015).
55. R. V. Raut, A. Z. Snyder, M. E. Raichle, Hierarchical dynamics as a macroscopic organizing principle of the human brain. *Proc. Natl. Acad. Sci. U. S. A.* **117**, 20890–20897 (2020).
56. A. Sans-Dublanc, *et al.*, Optogenetic fUSI for brain-wide mapping of neural activity mediating collicular-dependent behaviors. *Neuron* **109**, 1888-1905.e10

(2021).
57. R. G. Carson, Inter-hemispheric inhibition sculpts the output of neural circuits by co-opting the two cerebral hemispheres. *J. Physiol.* **598**, 4781–4802 (2020).
58. G. Pelled, *et al.*, Ipsilateral cortical fMRI responses after peripheral nerve damage in rats reflect increased interneuron activity. *Proc. Natl. Acad. Sci. U. S. A.* **106**, 14114–14119 (2009).
59. Y. Chen, *et al.*, Mapping the Brain-Wide Network Effects by Optogenetic Activation of the Corpus Callosum. *Cereb. Cortex* **30**, 5885–5898 (2020).
60. H. S. Moon, *et al.*, Contribution of Excitatory and Inhibitory Neuronal Activity to BOLD fMRI. *Cereb. Cortex* **31**, 4053–4067 (2021).
61. O. Detsch, E. Kochs, M. Siemers, B. Bromm, C. Vahle-Hinz, Differential effects of isoflurane on excitatory and inhibitory synaptic inputs to thalamic neurones in vivo. *Br. J. Anaesth.* **89**, 294–300 (2002).
62. M. Suzuki, M. E. Larkum, General anesthesia decouples cortical pyramidal neurons. *Cell* **180**, 666-676.e13 (2020).
63. A. Tauste Campo, *et al.*, Feed-forward information and zero-lag synchronization in the sensory thalamocortical circuit are modulated during stimulus perception. *Proc. Natl. Acad. Sci. U. S. A.* **116**, 7513–7522 (2019).
64. C. E. Landisman, B. W. Connors, VPM and PoM nuclei of the rat somatosensory thalamus: intrinsic neuronal properties and corticothalamic feedback. *Cereb. Cortex* **17**, 2853–65 (2007).
65. A. Kohn, *et al.*, Principles of corticocortical communication: proposed schemes and design considerations. *Trends Neurosci.* **43**, 725–737 (2020).
66. X. J. Wang, Macroscopic gradients of synaptic excitation and inhibition in the neocortex. *Nat. Rev. Neurosci.* **21**, 169–178 (2020).
67. Y. Li, *et al.*, Clonally related visual cortical neurons show similar stimulus feature selectivity. *Nature* **486**, 118–121 (2012).
68. S. Q. Ren, Z. Li, S. Lin, M. Bergami, S. H. Shi, Precise Long-Range Microcircuit-to-Microcircuit Communication Connects the Frontal and Sensory Cortices in the Mammalian Brain. *Neuron* **104**, 385-401.e3 (2019).
69. T. Tsurugizawa, D. Yoshimaru, Impact of anesthesia on static and dynamic functional connectivity in mice. *Neuroimage* **241**, 118413 (2021).
70. C. G. Cover, *et al.*, Whole brain dynamics during optogenetic self-stimulation of the medial prefrontal cortex in mice. *Commun. Biol.* **4**, 66 (2021).
71. W. B. Jung, H. Jiang, S. Lee, S. Kim, Dissection of brain-wide resting-state and functional somatosensory circuits by fMRI with optogenetic silencing. *Proc. Natl. Acad. Sci.* **119**, e2113313119 (2022).
72. K.-H. Chuang, *et al.*, Evaluation of nuisance removal for functional MRI of

rodent brain. *Neuroimage* **188**, 694–709 (2019).
73. Q. Wang, *et al.*, The Allen Mouse Brain Common Coordinate Framework: a 3D reference atlas. *Cell* **181**, 936-953.e20 (2020).

Acknowledgements

We thank Prof Linda Richards for helpful discussion and Ms Rowan Tweedale for proof reading. H.H.H. was funded by the Australian Research Council grant number DP180103319. K.H.C was supported by the startup funds from the Queensland Brain Institute and Centre for Advanced Imaging, The University of Queensland.

Funding:

Australian Research Council grant number DP180103319 (HHH).
Startup funds from the Queensland Brain Institute and Centre for Advanced Imaging, The University of Queensland, Australia (KHC).

Author contributions:

Conceptualization: KHC.
Methodology: KHC and HHH.
Investigation: KHC, HHH, SKG, ZL and DA.
Supervision: KHC.
Writing—original draft: KHC and HHH.
Writing—review & editing: KHC.

Competing interests:

Authors declare that they have no competing interests.

Data and materials availability:

The codes for data analysis and datasets generated in the current study are available from the corresponding author on reasonable request.

Figures

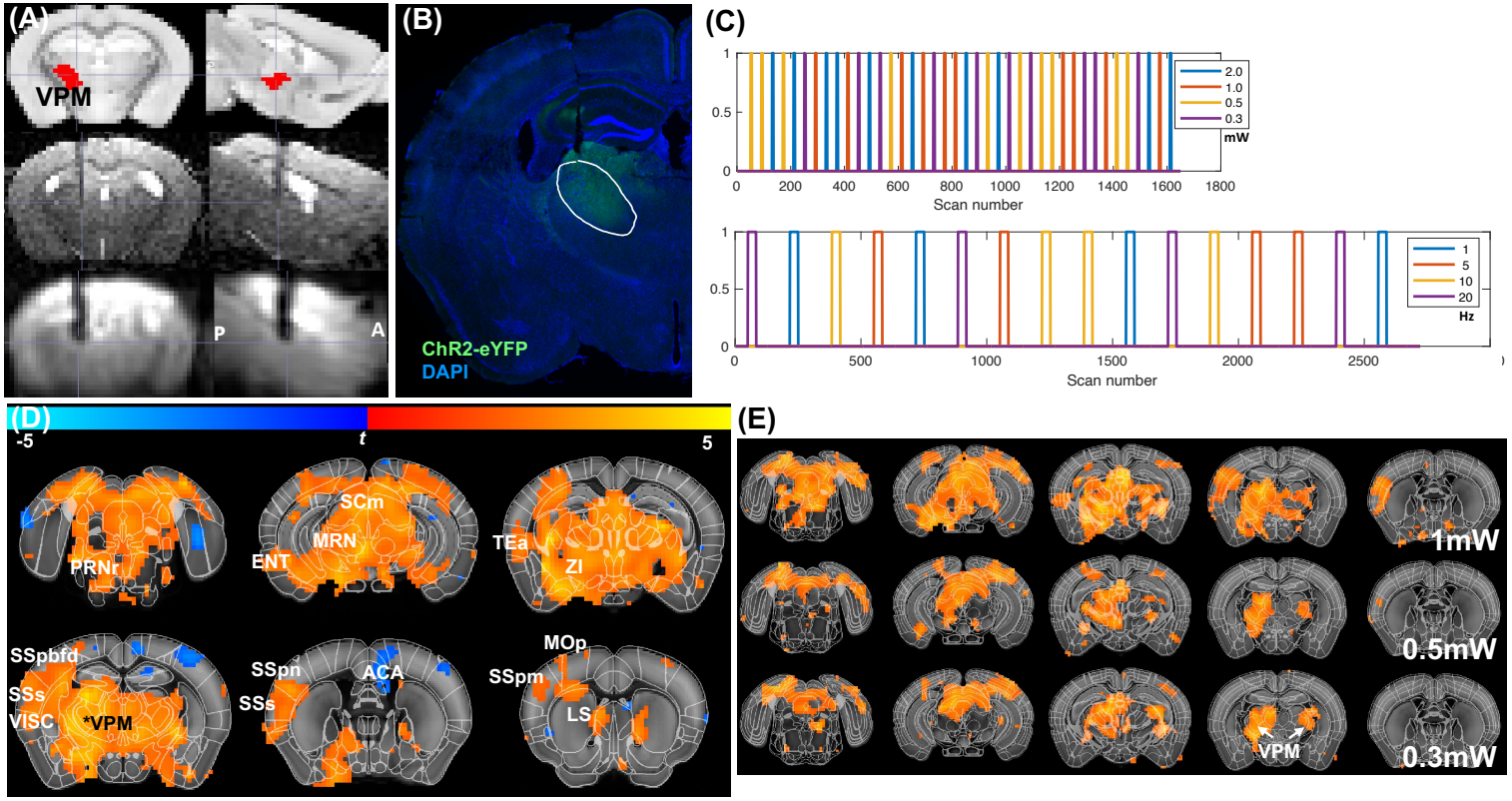

Fig. 1. Ultrafast fMRI detects brain-wide activation under optogenetic VPM excitation. (A) Brain atlas (top) and structural MRI (middle) shows fiber tract targeting to the VPM and the susceptibility artifact of the optic fiber in the simultaneous multislice EPI (bottom). **(B)** Histology shows ChR2 expression (green) together with DAPI (blue). **(C)** Event-related and block designs to measure the intensity- and frequency-dependent responses, respectively. **(D)** VPM excitation induces broad activation under 2mW stimulation power ($p<0.05$, FDR corrected). **(E)** The positive activated area reduces with lower stimulation power. See supplementary Table S2 for abbreviations of the brain region.

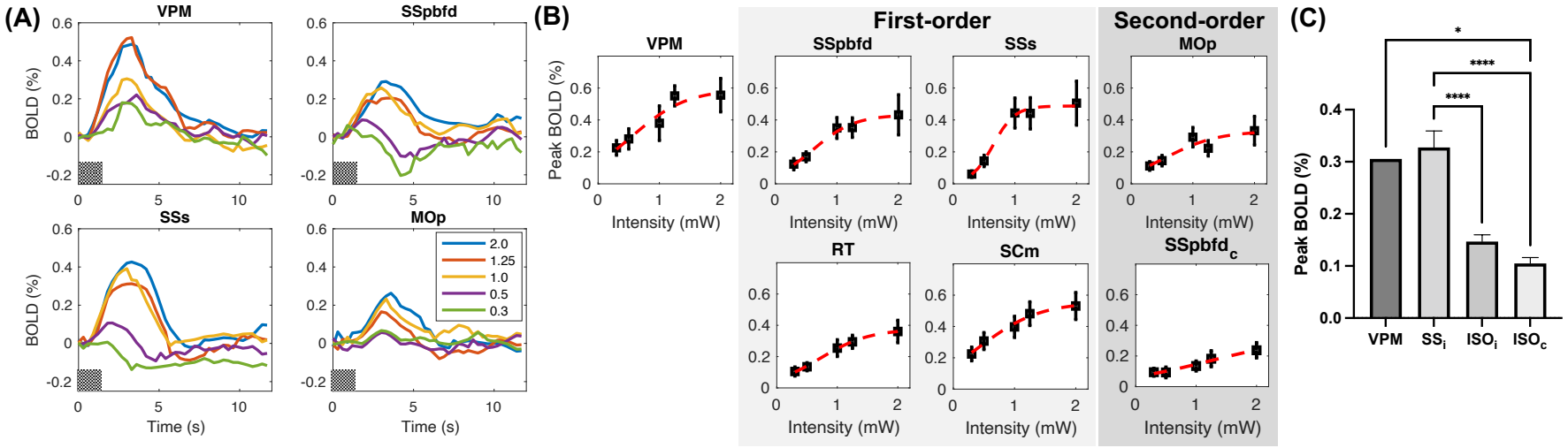

Fig. 2. Regional BOLD responses reduce with hierarchy. (A) Averaged BOLD signal time-courses in the VPM, two first-order afferent areas (SSpbfd and SSs) and a second-order area (MOp) under 5 stimulation intensities (in mW). The gray bar presents the stimulation period. **(B)** The stimulation intensity-dependent responsiveness follows a sigmoid function. Error bars present the SEM. **(C)** BOLD activation amplitudes are highest in the first-order areas and decrease in second-order isocortex (ISO) of the ipsilateral (ISO_i) and contralateral (ISO_c) hemispheres. *: $p<0.05$, ****: $p<0.0001$.

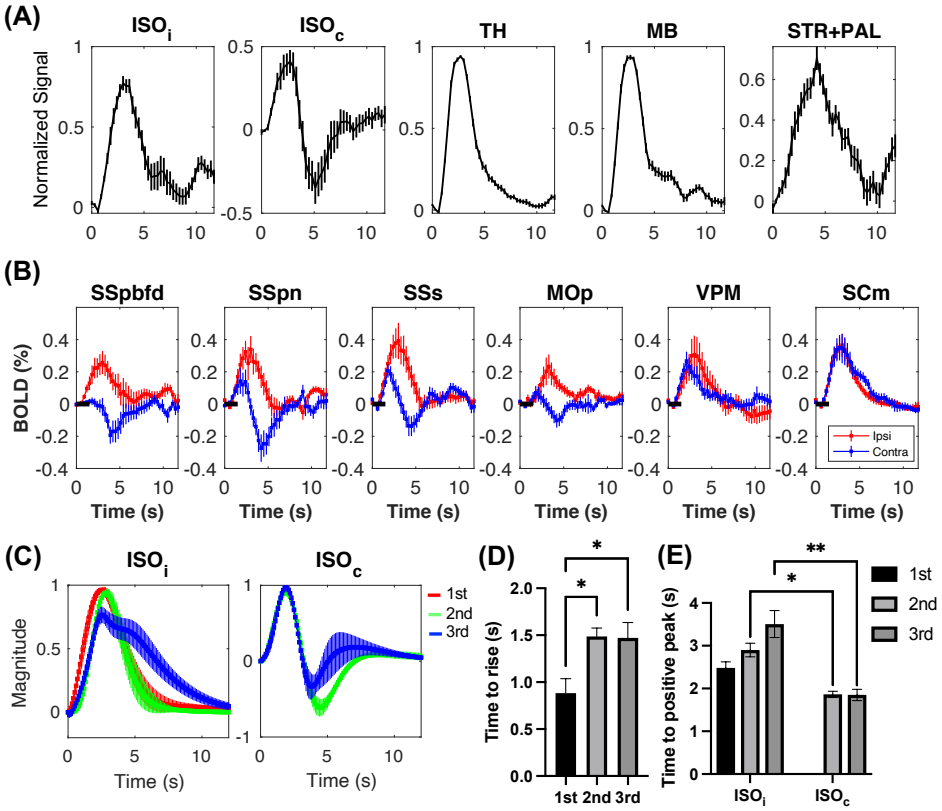

Fig. 3. Hemodynamics is region and hierarchy dependent. (A) Mean evoked BOLD of the ipsilateral and contralateral ISO, TH, MB, and STR+PAL measured at 1mW stimulation. **(B)** Examples of ipsilateral and contralateral BOLD responses in the somatosensory and primary motor cortices, and in the VPM and superior colliculus. The black bar represents the stimulation period. **(C)** Fitted hemodynamic responses over the three orders of major SC hierarchy in the ipsilateral and contralateral ISO. **(D)** The hemodynamic time-to-rise over hierarchy in the ipsilateral ISO. **(E)** The time-to-positive peak over hierarchy in the ipsilateral and contralateral ISO. *: $p<0.05$. Error bars represent the SEM.

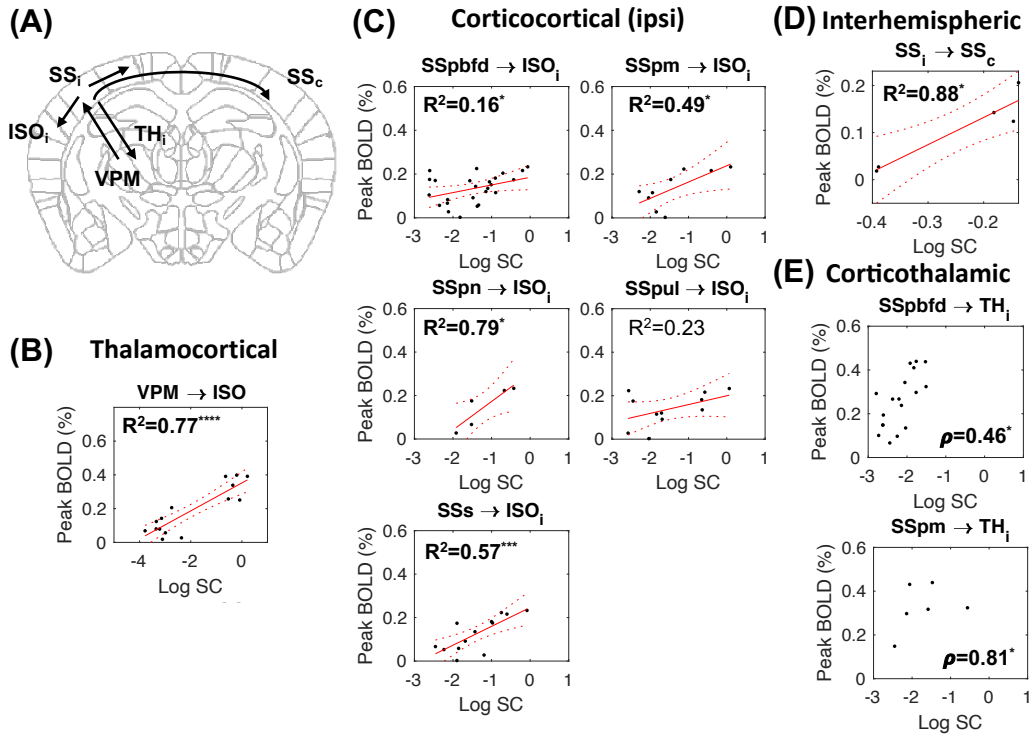

Fig. 4. BOLD activation correlates with SC. (A) Diagram of thalamocortical (VPM→ISO), corticocortical (SS_i→ISO_i, SS_i→SS_c) and corticothalamic (SS_i→TH_i) projections. Linear regression between the Log SC and the peak BOLD amplitude at the target areas measured at 1mW stimulation in the **(B)** thalamocortical feedforward, **(C)** corticocortical feedforward from the ipsilateral somatosensory cortex (SS_i) to ipsilateral ISO, and **(D)** corticocortical feedforward from the ipsilateral to contralateral somatosensory cortex (SS_c). **(E)** Spearman correlation between the Log SC and peak BOLD amplitude in the corticothalamic feedback from the somatosensory cortex to the ipsilateral thalamus. *: $p<0.05$, ***: $p<0.001$, ****: $p<0.0001$. Solid lines represent the linear fit and dashed lines represent the 95% confidence interval.

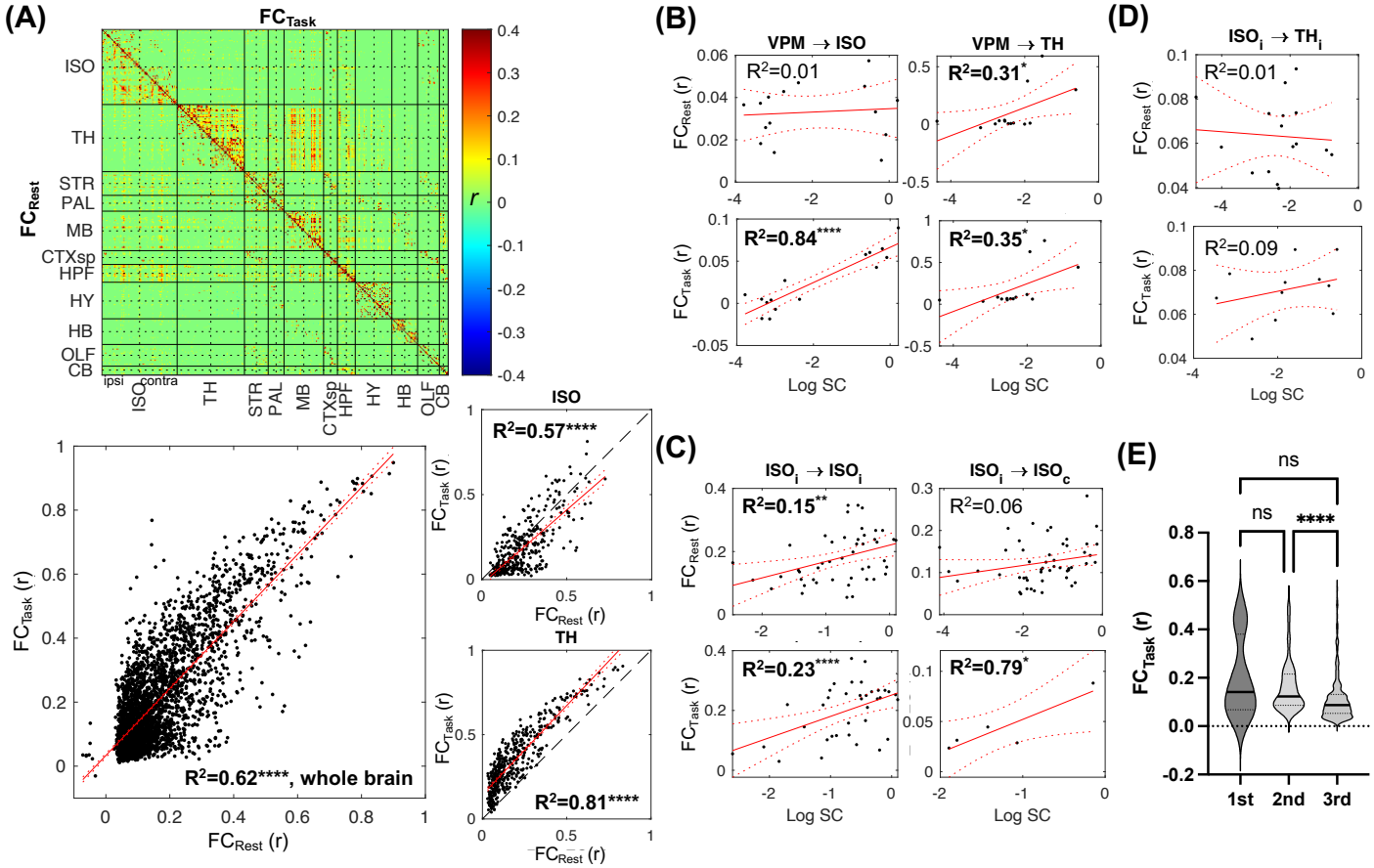

Fig. 5. Comparison between FC_{Rest}, FC_{Task} and SC. (A) The connectivity matrices of FC_{Rest} (lower triangle) and FC_{Task} (upper triangle) thresholded at $p<0.01$, and their correlation in the whole brain, ISO and TH. Linear regressions between the FC_{Rest} and Log SC (upper row) and between the FC_{Task} and Log SC (lower row) in the **(B)** thalamocortical and thalamic-thalamic feedforwards, (C) corticocortical feedforwards, and **(D)** corticothalamic feedback. **(E)** FC_{Task} over the hierarchy of major SC in the ipsilateral ISO. *: $p<0.05$, **: $p<0.01$, ***: $p<0.001$, ****:

$p<0.0001$. Dashed lines represent the 95% confidence interval. CTXsp: cortical subplate, HPF: hippocampal formation, HY: hypothalamus, OLF: olfactory bulb, CB: cerebellum.

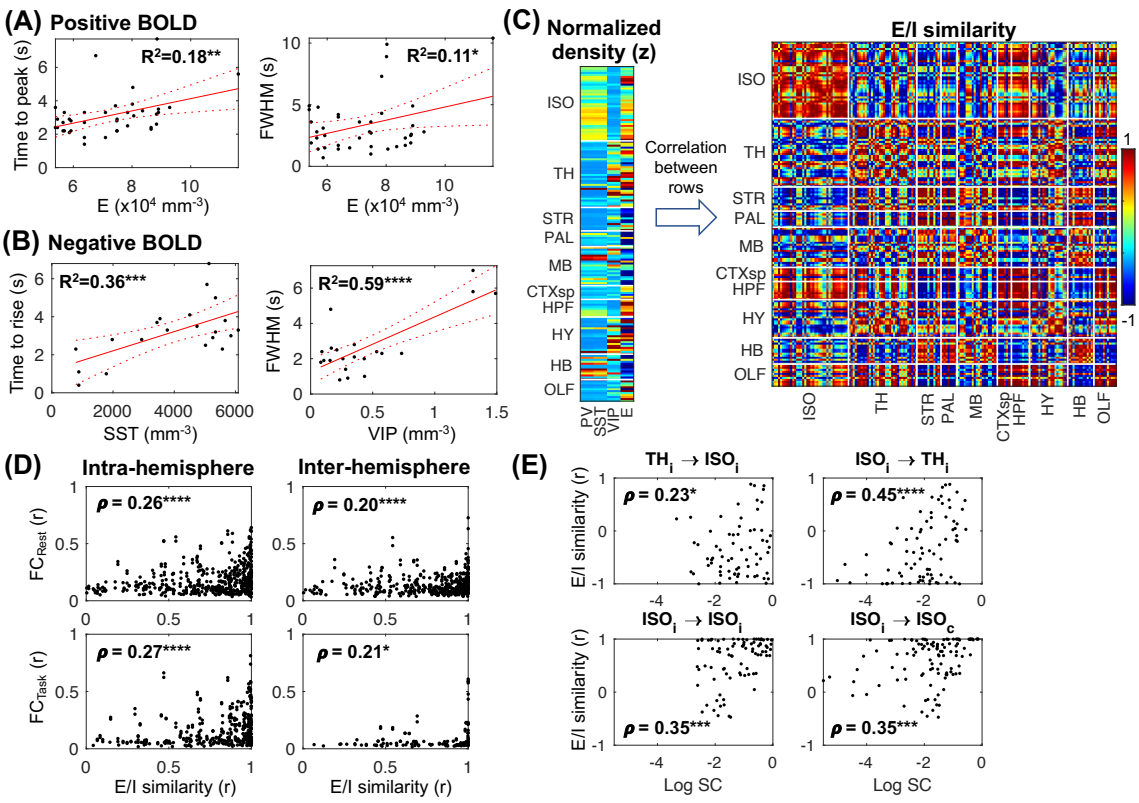

Fig. 6. Hemodynamics, FC and SC associated with E/I distribution. **(A)** The cortical hemodynamic time-to-peak and FWHM of the positive BOLD correlated with excitatory neuron density. **(B)** The cortical hemodynamic time-to-rise and FWHM of the negative BOLD correlate with inhibitory neuron density. **(C)** The normalized densities of 4 types of E/I neurons formed the E/I profile of each region. Inter-regional correlation of the E/I profiles shows highly similar distribution of the 4 neuron types within the ISO. **(D)** The intra- (left) and inter-hemispheric (right) cortical FC_{rest} (top) and FC_{task} (bottom) correlated with the E/I similarity. **(E)** E/I similarity correlated with SC in both feedforward and feedback projections.